1 **Estimation of secondary organic aerosol formation parameters for the**

2 **Volatility Basis Set combining thermodenuder, isothermal dilution**

3 **and yield measurements**

4 Petro Uruci[1,2], Dontavious Sippial[3], Anthoula Drosatou[1,2], and Spyros N. Pandis[1,2]

5 [1]Institute of Chemical Engineering Sciences (FORTH/ICE-HT), 26504, Patras, Greece
6 [2]Department of Chemical Engineering, University of Patras, 26500, Patras, Greece
7 [3]Department of Chemical Engineering, Carnegie Mellon University, Pittsburgh, USA

8 *Correspondence to*: Spyros N. Pandis (spyros@chemeng.upatras.gr)

9 **Abstract**

10 Secondary organic aerosol (SOA) is a major fraction of the total organic aerosol (OA)

11 in the atmosphere. SOA is formed by the partitioning onto pre-existent particles of low

12 vapor pressure products of the oxidation of volatile, intermediate volatility, and

13 semivolatile organic compounds. Oxidation of the precursor molecules results in a

14 myriad of organic products making the detailed analysis of smog chamber experiments

15 difficult and the incorporation of the corresponding results into chemical transport

16 models (CTMs) challenging. The volatility basis set (VBS) is a framework that has

17 been designed to help bridge the gap between laboratory measurements and CTMs. The

18 parametrization of SOA formation for the VBS has been traditionally based on fitting

19 yield measurements of smog chamber experiments. To reduce the uncertainty of this

20 approach we developed an algorithm to estimate the SOA product volatility

21 distribution, effective vaporization enthalpy, and effective accommodation coefficient

22 combining SOA yield measurements with thermograms (from thermodenuders) and

23 areograms (from isothermal dilution chambers) from different experiments and

24 laboratories. The algorithm is evaluated with "pseudo-data" produced from the

25 simulation of the corresponding processes assuming SOA with known properties and

26 introducing experimental error. One of the novel features of our approach is that the

27 proposed algorithm estimates the uncertainty of the predicted yields for different

28 atmospheric conditions (temperature, SOA concentration levels, etc.). The predicted

29 yield uncertainty is significantly less than that of the estimated volatility distributions

30 for all conditions tested.

1. Introduction

Submicrometer atmospheric particles are of great importance due to their negative effects on public health (Pope and Dockery, 2006; Lim et al., 2012) and their uncertain influence on Earth's climate (IPCC, 2013). Organic aerosol (OA) contributes 20–90 % to the submicron particulate mass (Zhang et al., 2007) and is emitted directly in the atmosphere as primary particles (POA) or formed as secondary organic aerosol (SOA). SOA constitutes a major fraction of the total OA in the atmosphere contributing more than 60 % on average (Kanakidou et al., 2005). SOA is formed by the condensation of low vapor pressure products of the oxidation of volatile (VOCs), intermediate volatility (IVOCs), and semi-volatile organic compounds (SVOCs).

Hundreds of mostly unknown products are formed during the oxidation of each SOA precursor making the detailed description of the corresponding reactions and eventual SOA formation extremely challenging. The volatility basis set (VBS) is one approach that has been proposed to simplify the system and to allow the SOA simulation in CTMs. The VBS describes the volatility distribution of OA using a set of surrogate species with effective saturation concentrations that vary by one order of magnitude (Donahue et al., 2006; Stanier et al., 2008). Volatility is one of the most important physical properties of SOA components as it determines to a large extent their gas-particle partitioning (Pankow, 1994a; 1994b). The parametrization of SOA formation for the VBS requires the determination of the yields of each volatility bin (volatility distribution of products) and the corresponding enthalpies of vaporization.

The SOA parametrizations for the VBS have been traditionally based on fitting yield measurements (Lane et al., 2008). The major weakness of this approach is that the resulting parametrization is limited to the range of OA concentrations and temperatures of the measurements. In most cases, the concentration range does not include the low concentrations relevant to the atmosphere and usually most of the experiments take place in a relatively narrow temperature range. Pathak et al. (2007a) needed 37 smog chamber experiments at different temperatures (0–45 ºC) and atmospherically relevant concentrations to constrain the α-pinene SOA temperature sensitivity.

A number of approaches has been used to minimize the number of experiments needed to characterize the temperature dependence of the SOA formation. Stanier et al. (2007) developed an experimental technique with which the temperature-controlled smog chamber could be heated or cooled after the SOA formation moving the system

66   to new equilibrium favoring evaporation or condensation respectively. However,

67   interactions of the SOA with the walls of the system increased the uncertainties of the

68   approach. Stanier et al. (2008) presented an algorithm to fit the smog chamber

69   experiments using several volatility bins. However, the number of experiments needed

70   by the algorithm should cover a wide range of concentrations and temperatures to

71   effectively constrain the stoichiometric mass yields and the effective vaporization

72   enthalpy.

73   In an effort to cover a wider concentration and temperature range,

74   thermodenuder measurements can be used. TD is a common instrument developed to

75   characterize the volatility of atmospheric aerosols by heating them and observing the

76   resulting changes in size, mass, optical properties, etc. (Burtscher et al., 2001; Wehner

77   et al., 2002, 2004; An et al., 2007). TDs consist of a heated tube in which the more

78   volatile particle components evaporate followed by a cooling section with activated

79   carbon to avoid vapor recondensation. The mass changes in TDs depend on the initial

80   SOA concentration, the residence time in the heating tube, the vaporization enthalpy,

81   and the mass transfer resistances. A typical way of reporting the TD measurements is

82   by calculating the aerosol mass fraction remaining (MFR) at a given temperature after

83   passing through the TD. The MFRs in a range of TD temperatures constitute the

84   thermogram.

85   In TD applications in the field (Cappa and Jimenez, 2010; Huffman et al., 2009;

86   Lee et al., 2010; Louvaris et al., 2017a) and in the laboratory (Kalberer et al., 2004;

87   Baltensperger et al., 2005; An et al., 2007; Lee et al., 2011; Cain et al., 2020) the system

88   does not reach equilibrium. Therefore, dynamic aerosol evaporation models (Riipinen

89   et al., 2010; Cappa, 2010; Fuentes and McFiggans, 2012) are needed for the

90   interpretation of TD measurements. Karnezi et al. (2014) used the time-dependent

91   evaporation model of Riipinen et al. (2010) to calculate the OA volatility distribution,

92   vaporization enthalpy, and mass accommodation coefficient from TD measurements.

93   The authors showed that a simple error minimization approach may not be appropriate

94   for such systems as very similar thermograms can be obtained for multiple

95   combinations of different parameters. For this reason, their approach estimates an

96   ensemble of "good" solutions, from which the best estimate and the corresponding

97   uncertainties are derived.

98   Grieshop et al. (2009) suggested the combination of TD and isothermal dilution

99   to constrain the volatility distribution of SOA. Karnezi et al. (2014) proposed an

100 algorithm to include both two types of measurements. The authors concluded that the

101 combination of the two type of measurements can better constrain the OA volatility

102 than each set separately. Louvaris et al. (2017b) and Cain et al. (2020) applied this

103 algorithm to cooking OA (COA) and SOA respectively. Louvaris et al. (2017b) showed

104 that the use of only TD measurements led to overestimation of the SVOC fraction of

105 COA, while the use of TD and isothermal dilution data reduces the uncertainty of the

106 volatility distribution and of the effective vaporization enthalpy. Cain et al. (2020)

107 obtained experimentally TD and isothermal dilution measurements for α-pinene and

108 cyclohexene ozonolysis SOA. The SOA in these two systems had similar thermograms,

109 but different areograms. When only thermograms were used in the model, the volatility

110 distributions were quite similar. However, the addition of areograms revealed that α-

111 pinene ozonolysis SOA consists mostly of LVOCs and the cyclohexene ozonolysis

112 SOA consists mostly of SVOCs.

113   To constrain the volatility product distribution of SOA and its effective

114 vaporization enthalpy we combine TD and isothermal dilution experiments with the

115 SOA yield measurements. We extend here the algorithm of Karnezi et al. (2014) by

116 introducing additional inputs (SOA yields) and also providing additional outputs

117 (uncertainty of estimated yields in relevant atmospheric conditions). The algorithm is

118 tested with "pseudo-experimental" data generated from the use of models simulating

119 the corresponding measurement processes, so the true parameters are known. The

120 results of the "pseudo-experiments" are corrupted so that they include experimental

121 errors.

122

123 **2. Model Description**

124 **2.1. SOA Formation**

125 Gas-phase oxidation of VOCs involves a large number of reactions and produces a large

126 number of products that can condense in the particulate phase. Depending on their

127 effective saturation concentration, they can be represented in the 1D-VBS framework

128 by

129 $$\text{VOC} + \text{oxidant} \rightarrow \alpha_1 P_1 + \alpha_2 P_2 + ... + \alpha_n P_n + \text{volatile products} \qquad (1)$$
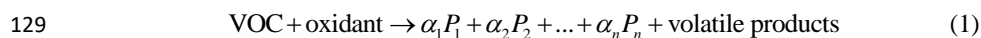
130 where n is the number of the surrogate compounds (volatility bins in the VBS), P_i is the

131 surrogate product in the i-th volatility bin and α_i is the corresponding stoichiometric

132 mass yield. The total SOA mass yield can be then calculated as:

133

$$Y \equiv \frac{C_{\mathrm{OA}}}{\Delta \mathrm{VOC}} = \sum_{i}^{n} \frac{\alpha_i}{1 + \left(C_i^* / C_{\mathrm{OA}}\right)} \quad (2)$$

134 where C_{OA} is the total SOA concentration, $\Delta \mathrm{VOC}$ is the consumed concentration of the

135 VOC and C_i^* is the effective saturation concentration of compound i. This yield

136 equation is an extension of the two-product model by Odum et al. (1996) replacing their

137 semi-empirical partitioning coefficients with the assumption of a pseudo-ideal solution

138 (Strader et al., 1999). This model assumes that the system has reached equilibrium when

139 the yield was measured and that the differences in molecular weights are small.

140   The effective saturation concentrations at different temperatures are given by

141 the Clausius-Clapeyron equation:

142

$$C_i^*(T) = C_i^*(T_{\mathrm{ref}}) \frac{T_{\mathrm{ref}}}{T} \exp\left[\frac{\Delta H_{\mathrm{vap},i}}{R}\left(\frac{1}{T_{\mathrm{ref}}} - \frac{1}{T}\right)\right] \quad (3)$$

143 where T_{ref} is the reference temperature in which the reference effective saturation

144 concentration is defined (298 K in this work), and $\Delta H_{\mathrm{vap},i}$ is the enthalpy of vaporization

145 of surrogate compound i.

146

147 **2.2. Thermodenuder Model**

148 The time-dependent evaporation of SOA in the TD is described in this work by the

149 dynamic mass transfer model of Riipinen et al. (2010). The evolution of the total

150 particle mass, m_{p}, and the gas phase concentration of the compound i, C_i are given by:

151

$$\frac{dm_{\mathrm{p}}}{dt} = -\sum_{i=1}^{n} I_i \quad (4)$$

152

$$\frac{dC_i}{dt} = I_i N_{\mathrm{tot}} \quad (5)$$

153 where n is the number of surrogate compounds, N_{tot} is the total number concentration

154 of particles (assuming monodisperse aerosol population) and I_i is the mass flux of

155 compound i from the gas to the particulate phase for each particle calculated by

156 (Seinfeld and Pandis, 2016):

157

$$I_i = \frac{2\pi d_{\mathrm{p}} M_i \beta_{\mathrm{mi}} D_i}{R T_{\mathrm{TD}}}\left(p_i - p_i^0\right) \quad (6)$$

158 where d_{p} is the particle diameter, R is the ideal gas constant, M_i is the molecular weight

159 of compound i, D_i is the diffusion coefficient of compound i in the gas phase at

160 temperature T_{TD}, p_i and p_i^0 are the partial vapor pressures of i far away from the particle

161 and at particle surface, respectively, and β_{mi} is a factor for the correction of kinetic and

162 transition regime effects (Fuchs and Sutugin, 1970):

$$\beta_{mi} = \frac{1 + Kn_i}{1 + \left(\dfrac{4}{3\alpha_{mi}} + 0.377\right)Kn_i + \dfrac{4}{3\alpha_{mi}}Kn_i} \tag{7}$$

164 where Kn_i is the Knudsen number of compound i, and α_{mi} is the mass accommodation

165 coefficient of compound i on the particles. The partial vapor pressure of compound i at

166 the particle surface is given by:

$$p_i^0 = x_{mi}\frac{C_i^* RT}{M_i}\exp\left(\frac{4M_i\sigma}{RT_{TD}\rho d_p}\right) \tag{8}$$

168 where x_{mi} is the mass fraction of compound i in the particulate phase, C_i^* is the effective

169 saturation concentration, σ is the surface tension (assumed 0.05 N m^{-1} in our

170 simulations), T_{TD} is the particle temperature assumed to be the same as in the TD, and

171 ρ is the particle density. The effective saturation concentrations at different TD

172 temperatures are given by Eq. (3).

173

2.3. Isothermal Dilution Model

175 In isothermal dilution experiments, a SOA sample is injected in a reactor filled with

176 clean air at room temperature. The concentrations of both the gas and particulate phase

177 components are lowered due to dilution leading the system out of equilibrium. The

178 evaporation of SOA as a result of isothermal dilution is also described by equations (3)-

179 (8) (Karnezi et al., 2014), but the temperature is equal to 298 K. Evaporation in a

180 dilution chamber depends on the initial SOA mass, time, and the α_m, but not on ΔH_{vap}

181 as the particles evaporate without a change in temperature.

182

3. Algorithm for the Estimation of VBS Parameters

184 The algorithm of Karnezi et al. (2014) was first extended to include an SOA partitioning

185 model together with the TD and isothermal dilution models in order to estimate the

186 volatility product distribution, vaporization enthalpy and accommodation coefficient.

187 We discretized the domain of the parameters and simulated all combinations of

188 stoichiometric mass yields (α_i), ΔH_{vap}, and α_m. The yields α_i were allowed to vary from

189 0.0 to 0.8, with values of 0.0, 0.05, 0.1, 0.15, 0.2, 0.3, 0.4, 0.6, and 0.8. Combinations

190 with sum of the yields exceeding 1.0 were excluded from the analysis. For a 4-product

191   system there are 3,153 and for a 6-product system 66,636 acceptable combinations. The

192   values used for ΔH_{vap} were from 20 to 200 kJ mol^{-1} with a step of 20, and for α_m, the

193   values used were 0.001, 0.01, 0.1, and 1. As a result 126,120 simulations are needed

194   for a 4-product VBS and 2,665,440 for a 6-product solution.

195   For each simulation and each type of measurement, we calculated the

196   *normalized mean square error* (NMSE) defined as

197

$$\text{NMSE} = \frac{\sum_{i=1}^{N_O} (P_i - O_i)^2}{\sum_{i=1}^{n} O_i} \tag{9}$$

198   where O_i represents the ith observed value (corresponding to a specific SOA

199   concentration for yield measurements or temperature for TD, or time for isothermal

200   dilution), P_i the corresponding model-predicted value, and N_O is the total number of

201   observations from each type of measurement. For each simulation (denoted as s), the

202   overall error was calculated by assuming equal weight to the set of yield, TD, and

203   dilution measurements and summing the corresponding errors:

204     $$E_s = \text{NMSE}_{Y,s} + \text{NMSE}_{TD,s} + \text{NMSE}_{Dil,s} \tag{10}$$

205   The parameter combinations for which the overall error E_s is less than 5% are

206   identified. The best solution is then calculated by averaging these solutions using the

207   inverse error E_s as a weighting factor. The solutions that are closer to the measurements

208   have higher weight. More specifically the best estimate $\bar{x}$ is given by:

209

$$\bar{x} = \frac{\sum_{k}^{N} x_k \frac{1}{E_k}}{\sum_{k}^{N} \frac{1}{E_k}} \tag{11}$$

210   where x_k is the estimated value of a property (mass yield of a volatility bin, effective

211   vaporization enthalpy, or effective accommodation coefficient) and N is the number of

212   combinations with error below the threshold value. The uncertainty range of the

213   parameters is estimated by calculating the standard deviation (σ):

214

$$\sigma = \sqrt{\frac{\sum_{k}^{N} \left[(x_k - \bar{x})^2 \cdot \frac{1}{E_k} \right]}{\sum_{k}^{N} \frac{1}{E_k}}} \tag{12}$$

215   following Karnezi et al. (2014).

216

4. Testing of the Algorithm

4.1. Generation of Data for Evaluation

219 In order to evaluate the algorithm, we generated data using the output of SOA

220 formation, thermodenuder and isothermal dilution models for systems with known

221 volatility distribution of the products, and properties. Then, these data were "corrupted"

222 with random errors to represent the "noise" observed in laboratory measurements for

223 yields, thermograms, and areograms. The yields were corrupted based on the variability

224 of laboratory measurements of Pathak et al. (2007a), by assuming a normal distribution

225 and standard deviation (σ_Y) given by:

226
$$\sigma_Y = 0.1 Y_{\text{true}} + 0.02 \tag{13}$$

227 where Y_{true} are the correct yields.

228 For TD, the errors were calculated by assuming a normal distribution and the

229 standard deviation (σ_{TD}) suggested by Karnezi et al. (2014):

230
$$\sigma_{\text{TD}} = 0.51 MFR_{\text{TD,true}} - 0.5 \left(MFR_{\text{TD,true}} \right)^2 \tag{14}$$

231 where $MFR_{\text{TD,true}}$ are the correct MFR values for each TD temperature.

232 For dilution, the errors were calculated by assuming a uniform distribution and

233 standard deviation (σ_{Dil}) suggested by Karnezi et al. (2014):

234
$$\sigma_{\text{Dil}} = 0.05 \, MFR_{\text{Dil,true}} + 0.03 \tag{15}$$

235 where $MFR_{\text{Dil,true}}$ are the correct MFR values for isothermal dilution.

236 Based on the above methodology, we generated "pseudo-measurements" of

237 yield, TD, and isothermal dilution for different SOA systems. The parameters used to

238 produce the pseudo-experimental data are summarized in Table S1. The "experimental"

239 conditions assumed for the TD and isothermal dilution measurements are shown in

240 Table S2.

241 In "Experiment" A, we test the performance of the algorithm against α-pinene

242 ozonolysis data and examine the effect of TD and isothermal dilution data. For

243 "Experiment" A, the "true" values were taken from the parameterization derived by

244 Pathak et al. (2007b) for the ozonolysis of α-pinene at low NO$_x$, dark and low RH

245 conditions. So these results are good fits of the measurements analyzed in that study.

246 The parametrization was derived assuming a 4-volatility bin system with saturation

247 concentrations ranging from 1 to 10^3 µg m^{-3}. The effective vaporization enthalpy

248 estimated in that study was equal to 30 kJ mol^{-1}. Because the effective accommodation

249 coefficient was not part of the Pathak et al. (2007b) parametrization, we assumed a

250 value of 0.5 in this work. We used a small number of yield measurements at

251 atmospherically relevant SOA concentrations of 1, 5, 10, 20 and 40 µg m^{-3} (Fig. 1). For

252 this SOA system, the yield at 40 µg m^{-3} did not exceed 20%. The thermogram includes

253 ten MFR data points in the temperature range of 20 to 200 °C. For the highest

254 temperature, more than 70% of the SOA mass was evaporated. The areogram shows

255 that the correspondent SOA evaporated almost by 70 % in the first 0.5 h and more than

256 90% in less than 3 h.

257   For "Experiment" B, the "true" values were taken from the alternative

258 parametrization proposed by Pathak et al. (2007b) for the same oxidation system as

259 described before. This time, the authors used a 7-volatility bin system with saturation

260 concentrations ranging from 10^{-2} to 10^{4} µg m^{-3} in their parametrization. The effective

261 vaporization enthalpy of the parametrization was 30 kJ mol^{-1}, while for the

262 accommodation coefficient we assumed again a value of 0.5. The yield, TD and

263 isothermal dilution "measurements" of Experiment B are generated in the same SOA

264 mass concentration, temperature, and dilution time range as in the previous pseudo-

265 experiment (Fig. 2).

266   For "Experiment" C, the "true" values were based on the parameterization of

267 the SOA formed during α-humulene ozonolysis by Sippial et al. (2022). The authors

268 measured high SOA yields for α-humulene in the main smog chamber (~70% at 60 µg

269 m^{-3}), and their corresponding thermogram suggested that the SOA particles fully

270 evaporated at 150 °C, while the areogram showed modest (20%) evaporation in the

271 dilution chamber after 3 hours. A 4-volatility bin set with saturation concentrations

272 ranging from 10^{-2} to 10 µg m^{-3} was used in that study to fit the measurements. The

273 stoichiometric coefficients of the three least volatile bins (10^{-2}, 10^{-1} and 1 µg m^{-3}) were

274 around 0.1 and for the most volatile (10 µg m^{-3}) 0.25. The vaporization enthalpy was

275 115 kJ mol^{-1} and the accommodation coefficient was 0.01 (Table S1). We assumed five

276 yield "measurements" in the SOA concentration range of 1 to 100 µg m^{-3} with yield

277 values as high as 65 % at 100 µg m^{-3} (Fig. 3). The corresponding thermogram consisted

278 of 10 data and the particles fully evaporated at TD temperatures higher than 150 °C.

279 The areogram consisted of 17 data points and only 20 % of the SOA evaporated in the

280 dilution chamber.

281

4.2. Parameter Estimation for "Experiments" A, B, and C

We explored the performance of the algorithm for different choices of the number of volatility bins, the range of saturation concentrations, and the range of SOA mass concentration range in the yield measurements. For each test, the "true" and the estimated properties are summarized in Table 1.

We evaluated the performance of our parameter estimation algorithm comparing its predictions both against the "measurements" and also against the "truth" defined as the predictions of the original parameterization. In both comparisons, *mean normalized error* (MNE) (Emery et al., 2017) was used as metric.

For the evaluation against the "measurements", the MNE_M was defined as

$$MNE_M = \frac{100}{N_O} \sum_{i=1}^{N_O} \frac{\left| EST_i - O_i \right|}{O_i} \qquad (16)$$

where EST_i is the estimated by the algorithm value and corresponds to a specific measured point O_i.

For the evaluation against the "truth", which includes conditions (e.g., temperatures or concentrations) for which there are no available measurements, the MNE_T was defined as:

$$MNE_T = \frac{100}{N_d} \sum_{j=1}^{N_d} \frac{\left| EST_j - TR_j \right|}{TR_j} \qquad (17)$$

where EST and TR are the estimated and the "true" values respectively. N_d is the total number of data points included in calculations and depends on the selected discretization of the corresponding dependent variable (e.g., SOA concentration, TD temperature, and dilution time). We used a linear discretization for the SOA concentrations (from 0.01 to 50 µg m^{-3} with a step of 0.01) and the TD temperatures (20 to 200 °C with a step of 5 °C but including TD MFR values greater than zero). For the dilution time, we used a higher resolution for the first 0.5 hour (step of 2 min), in which the evaporation is usually faster, and lower then (step of 10 min) up to 3 hours.

Finally, we used the average relative standard deviation (*ARSD*) as a metric to quantify the uncertainty of the estimates (range of good solutions) using the same discretization as in the MNE_T metric. The *ARSD* is given by:

$$ARSD = \frac{100}{N_d} \sum_{j=1}^{N_d} \frac{\sigma_j}{EST_j} \qquad (18)$$

where σ_j is the standard deviation for data point j.

4.2.1 Parameter Estimation for "Experiment" A

312   In Test A1, we applied the algorithm in the same range of saturation concentrations and

314   with the same number of volatility bins as these used to produce the "experimental"

315   data. The upper bin (10^3 µg m^{-3}) exceeded the maximum SOA concentration (40 µg

316   m^{-3}) in the measurement range by one order of magnitude.

317   Figure 1 depicts the estimated and the range of the ensemble of best solutions

318   for the three types of "measurements" for Test A1. The performance of the model for

319   the yields at 25 $^{\circ}$C was quite encouraging with a small tendency of overprediction for

320   SOA higher than 10 µg m^{-3}. The MNE_{M} of the model for the SOA yield "measurements"

321   (given by Eq. 16) was equal to 25% (Table 2). The corresponding discrepancy between

322   the true parameterization and the measurements (due to the measurement error that we

323   introduced) was 21.2% (Table 2). This indicates that a significant part of the algorithm

324   error can be explained by the uncertainty introduced in the measurements.

325   Our algorithm can be used to calculate the SOA yield at different concentrations

326   and temperatures. The yields were calculated in the atmospherically relevant range of

327   0–50 µg m^{-3} SOA concentration and at four temperatures (5, 15, 25, and 35 $^{\circ}$C) using

328   the true parameter values and the estimated parameters of Test A1. At 25 $^{\circ}$C, the

329   estimated yield curve is in good agreement with the "true" yield curve for SOA

330   concentrations lower than 6 µg m^{-3} (error of 8% at 6 µg m^{-3}), but the discrepancies

331   increase at higher concentrations (error of 23% at 50 µg m^{-3}). The average MNE_{T} error

332   between the true parametrization and the estimated values (given by Eq. 17) was equal

333   to 17.3% for yields at 25 $^{\circ}$C (Table 3). The uncertainties, as expected, are larger at lower

334   temperatures. However, the MNE_{T} error (estimated yields compared to the true value)

335   remains less than 25% (Table 3) even at 5 $^{\circ}$C, quite far from the measurement

336   temperature.

337   The algorithm provides a range of "good" estimates in addition to the best

338   estimate. The range can be defined by the lower and upper SOA yield limits of the

339   ensemble of the good solutions at each point. At 25 $^{\circ}$C, the yield range increased, as

340   expected, at higher concentrations (yield range of 0.05 at 1 µg m^{-3} to 0.17 at 50 µg

341   m^{-3}). The average relative standard deviation ($ARSD$ of the estimated yields defined by

342   Eq. 18) was equal to 26% (Table 4) for the 25 $^{\circ}$C case. For the rest of the temperatures,

343   the $ARSD$ increased for the lower temperatures, ranging from 24% at 35 $^{\circ}$C to 35% at

344   5 $^{\circ}$C (Table 4) and including in all cases the true solution.

345   For the TD, the model reproduced well the correspondent thermogram with low

346   errors compared to the "measurements" with an error MNE_M of 7% (Table 2). The error

347   MNE_T compared to the "true" values was 5.5% (Table 3). The error of the TD

348   "measurements" compared to the true values was equal to 7.6% (Table 2). Therefore,

349   the error of the proposed algorithm is quite similar to the experimental error. The error

350   introduced into the "measurements" was transferred, as expected, to the error metrics

351   of the algorithm.

352   For the isothermal dilution, the algorithm did reasonably well for the first 30

353   minutes and then the evaporation was slightly underpredicted leading to an error MNE_M

354   of 16.7% (Table 2). This MNE_M value was roughly two times higher than the

355   corresponding error between the dilution measurements and the true parametrization

356   (Table 2). The error between the estimated and the "true" values MNE_T was 19%. The

357     $ARSD$ of 24% (Table 4) was sufficient to include the true solution.

358   The estimated volatility distribution of the products and the effective

359   vaporization enthalpy and accommodation coefficient using the three types of

360   measurements can be seen in Figure 4 and Table 1. The estimated volatility distribution

361   of the products was in a good agreement with the "true" values (α_i absolute difference

362   of 0.01 at 1 µg m^{-3}, 0.03 at 10 µg m^{-3}, 0.07 at 10^2 µg m^{-3}, and 0.04 at 10^3 µg m^{-3}) and

363   the estimated uncertainties contained the correct values. There is a large uncertainty

364   range for the two higher volatility bins (standard deviation higher than 0.13) indicating

365   that yield values at a wider range of SOA concentrations would be needed to better

366   constrain these volatility bins. The relative error of the estimated ΔH_{vap} is 10%. The

367   estimated accommodation coefficient was 0.17 compared to a true value of 0.5. The

368   estimated uncertainty for the effective accommodation was almost one order of

369   magnitude (from 0.06 to 0.51) indicating the difficulty of constraining this parameter

370   when it is close to unity and thus the resistances to mass transfer are small.

371

4.2.2 Parameter Estimation for "Experiment" B

373   In this section, we used the pseudo-experimental data of Experiment B, which were

374   obtained for an SOA system with more components and a much wider range of

375   volatilities including LVOCs, SVOCs and IVOCs (10^{-2}–10^4 µg m^{-3}). In Test B1, the

376   algorithm was applied using a 4-bin VBS with saturation concentrations ranging from

377   1 to 10^3 µg m^{-3}. This range is narrower than the actual range used to obtain the pseudo

378   measurements of Experiment B.

379   Figure 2 shows the results of the fitting for the three types of "measurements"

380   in this experiment. At 25 °C, the model performance for the yields is encouraging

381   (MNE_M=20.6%). This is again pretty close to the measurement error (20.5%). By

382   comparing the estimated and the "true" yield curves at 25 °C, the error MNE_T is now

383   14%. The error increases to 31% at 5 °C, far from the available measurements. This is

384   reflected also in the increase of the uncertainty of our estimates with the $ARSD$

385   increasing from 17% at 35 °C to 37% at 5 °C (Table 4). Once more the uncertainty

386   range estimated by the algorithm includes the true values.

387   Both "measured" and "true" thermogram were well captured by the best

388   estimate (MNE_M of 6% and MNE_T of 4%) with an uncertainty $ARSD$ of 20.5%. The

389   evaporation in the dilution chamber was a little underestimated for the first 2 h, but then

390   it was slightly overpredicted. The MNE_T for the areogram was 13.3% and the true values

391   were included within the range of the estimates ($ARSD$ of 18%).

392   Figure 5 shows the results of Test B1 for the volatility distribution of the

393   products. The "true" stoichiometric coefficient for the 1 μg m^{-3} bin was overestimated

394   by 0.01 by the algorithm. This overestimation actually corresponds to the total material

395   of the 10^{-2} and 10^{-1} μg m^{-3} bins of the "true" system. This indicates that the algorithm

396   places the material of the two lowest bins that are not part of the solution to the bin with

397   the lower volatility. For the 10 μg m^{-3} and 10^2 μg m^{-3} bins, the relative errors between

398   the estimated and "true" were 58% and 277% respectively (Table S3), while for the 10^3

399   μg m^{-3} bin, the relative error was 10 %. The ΔH_{vap} was predicted accurately (error of

400   only 4%), while α_m was underpredicted (0.1 instead of 0.5).

401   The results of Test B1 suggest that the mismatch between the actual SOA

402   volatility distribution and the range used for the fits can introduce significant errors in

403   the retrieved distribution for individual volatility bins. However, despite these problems

404   the yields predicted by the derived parameterizations have a much lower error than the

405   volatility distribution. This is a valuable insight for the strengths and weaknesses of this

406   and other similar SOA parameter estimation algorithms.

407

408   4.2.3 Parameter Estimation for "Experiment" C

409   In Test C1, we obtained the best fits for the pseudo-measurements of Experiment C by

410   applying the algorithm in the same range of saturation concentrations and with the same

411   number of volatility bins (4 volatility bins in the 10^{-2}–10^1 μg m^{-3} saturation

412   concentration range) as the true volatility distribution.

413   Figure 3 shows the results of the fitting for the three types of "measurements".

414 The best estimate for the SOA yields at 25 °C was in a good agreement with the

415 "measurements" (MNE_M=6.3%) and the "true" values (MNE_T=9.6%). For the rest of

416 the temperatures, there was a decreasing trend of the error as the temperature decreased

417 varying from 15.5% at 35 °C to 6.2% at 5 °C. A similar decreasing trend was observed

418 for the uncertainty $ARSD$ of the estimates which varied from 23% at 35 °C to 15% at 5

419 °C. This behavior is the opposite from what we observed in the previous tests, in which

420 both errors and uncertainties increased at lower temperatures. However, the changes in

421 both the error and the uncertainty are small (change of around 7% between the upper

422 and lower temperature for both metrics), indicating that this system is less temperature-

423 sensitive in this temperature range than the previous ones.

424   The performance of the algorithm was satisfactory compared to the TD

425 "measurements" (MNE_M=12.9%). The corresponding error of the algorithm for the true

426 values (MNE_T) was 4.4% for temperatures up to 110 °C and equal to 10.6% for the

427 lower values at higher temperatures. According to Figure 3, the evaporation due to

428 dilution was initially overestimated for the first 30 min, but then underestimated

429 (highest MFR discrepancy of 0.05) and there is a high uncertainty range of the

430 corresponding estimates (MFR range of 0.46 at 3 h). However, the low dilution values

431 resulted in low relative errors (MNE_M of 3.5% and MNE_T of 2.7%).

432   Figure 6 shows that the highest relative errors were calculated for the 10^{-1} and

433 10^0 µg m^{-3} bins (23% and 33% respectively), and smaller relative errors for the other

434 two bins (less than 13%). The uncertainties were almost of the same magnitude for all

435 bins with standard deviations ranging from 0.09 to 0.13. The performance of the model

436 was good for the ΔH_{vap} (relative error of 7%), but with high uncertainty for α_m.

437

438 **4.3. Effect of the Volatility Range**

439 In in this section, we explore the performance of the algorithm for different choices of

440 the number of volatility bins and the range of saturation concentrations. The analysis

441 of the results of Test B1 has already quantified the effects of using a narrower volatility

442 distribution in the parameter estimation algorithm than the one of the investigated SOA

443 system. Additional sensitivity tests are performed here for all cases.

444   In Test A2, we used 3 volatility bins covering the 1–10^2 µg m^{-3} saturation

445 concentration range instead of the 4 bins used in Test A1 and covering the 10^3 µg m^{-3}

446 material. The narrower assumed volatility range had a very small effect on the estimated

447   yields at all temperatures (Table 3 and Fig. S1) compared to Test A1. The change in

448   MNE_T ranged from 3% at 5 °C to 0.3% at 35 °C. Minor changes were detected in the

449   predicted thermogram (change of 0.8%) and areogram (change of 0.5%) as well. The

450   uncertainty of the yield estimates increased by less than 2.5% at all temperatures. The

451   estimated volatility distribution of the SOA products of Test A2 changed by less than

452   5% in the two lower bins. The material in the 10^2 µg m^{-3} increased by 15% to account

453   for the SOA of higher volatility that could not be included otherwise in the estimated

454   distribution. The estimated ΔH_{vap} was in this case 32 kJ mol^{-1} (2.7% decrease) and the

455   α_m decreased by 12% with respect to Test A1.

456   In Test A3, we shifted the assumed 4-bin volatility distribution by one order of

457   magnitude to lower values, covering in that way the 0.1–100 µg m^{-3} saturation

458   concentration range. In this case, the algorithm distributed exactly the same material to

459   the 1, 10 and 100 µg m^{-3} volatility bins as in Test A2, and it predicted correctly zero

460   SOA in the 0.1 µg m^{-3} bin (Table 1). The ΔH_{vap} and α_m estimated values were also

461   unchanged with respect to Test A2. This in turn, led to the same estimated yields at

462   different temperatures (no change in the error between the two tests).

463   In Test C2, we applied the algorithm against the Experiment C "measurements"

464   using a 4-volatility bin system in the 1 to 10^3 µg m^{-3} range, that is two orders of

465   magnitude higher than the actual range of the "true" values. Figure 7 shows the results

466   of the fitting for the three types of "measurements". Despite the significant mismatch

467   of the volatility distributions the MNE_M increased by only 2.3% for the estimated SOA

468   yields. The error for the TD measurements increased by 20% while it actually decreased

469   a little (1.2%) for the dilution data. The errors compared to the true values increased by

470   less than 3% for the temperature range 15–35 °C while it increased by 12% at 5 °C.

471   These results suggest that the estimated yields are quite robust in this case to the

472   assumed volatility range. The major effect of the mismatch in volatility ranges was

473   evident in the predicted thermogram with overestimation of the MFR for the 60–120

474   °C temperature range and underprediction in higher temperatures. The increase in

475   MNE_T for the TD MFR was 17.2% (Table 3). The change in the predicted areogram

476   was marginal and led to a small increase of MNE_T (error increase by 0.7%) (Table 3).

477   The algorithm underestimated again the α_m (0.004 instead of 0.01) but also recognized

478   the high uncertainty of the corresponding estimate. The algorithm distributed

479   significant material to the 1 µg m^{-3} bin (3.6 times higher than the actual), in an effort to

480   account for the absence of the 10^{-2} and 10^{-1} µg m^{-3} bins. The ΔH_{vap} was underestimated

481   with an error of 21%.

482   The results of the above tests indicate that a mismatch between the true and

483   assumed volatility ranges of the SOA increases in general the estimation error but the

484   increase is small to modest. This is reassuring for the robustness of the proposed

485   algorithm.

486

487   **4.4. Effect of Measurements at high SOA Levels**

488   During the last decade there has been a significant shift of the performed SOA smog

489   chamber towards lower SOA concentrations. This is needed to increase the accuracy at

490   the ambient concentration levels. The high SOA concentration experiments that once

491   represented the majority of the performed experiments are becoming increasingly rare.

492   In this paragraph we examine the value of these high concentration experiments for the

493   estimation of SOA yields at ambient conditions.

494   To examine the effect of "measurements" at SOA levels much higher than the

495   atmospheric ones, we included an extra yield measurement at 200 µg m^{-3} in the yield

496   data of Experiments A and B. In Test A4 and B2, we applied the algorithm once again

497   against the three types of "measurements" by using a 4-volatility bin system with

498   saturation concentrations ranging from 1 to 10^3 µg m^{-3}.

499   In Test A4, the additional experiment at high SOA concentration led to an MNE_T

500   of 15.7% for the yields at 25 °C (Table 3 and Fig. S2), which is by 1.6% lower than that

501   without this experiment in Test A1. The improvement was more significant at lower

502   temperatures e.g., the MNE_T at 5 °C was reduced from 24.4% to 20.4%. The reduction

503   in the $ARSD$ for the SOA yields ranged from 3.8% at 5 °C to 0.9% at 35 °C (Table 4).

504   Figure 8 depicts the results of the model for the yields and the volatility distribution of

505   the products for Test A4. The accuracy of the predicted volatility distribution increased

506   especially for the higher volatility material. For example, the error for the 10^2 µg m^{-3}

507   bin was reduced from 41% in Test A1 to 6% in this case (Table S3). Minor changes in

508   the errors were detected for the ΔH_{vap} and α_m between the two tests (3% increase and

509   6% decrease respectively).

510   Similar to Test A4, in Test B2 we added a yield measurement at 200 µg m^{-3} in

511   the Experiment B set of "measurements". Figure 9 depicts the results of the model for

512   the SOA yields at 25 °C and the estimated volatility distribution of the products. The

513   use of the additional data point led to a reduction of the NME_T from 13.9% in Test B1

514   to 9% in Test B2 at 25 °C (Table 3). Similar reductions in the NME_T were observed for

515   the other temperatures, with the highest one observed at 5 °C (lower error by 7%)

516   (Figure 10). The reduction in the $ARSD$ for the estimated yields ranged from 3.3% at 5

517   °C to 1.2% at 35 °C (Table 4). Minor changes were observed for the estimated

518   thermogram (Fig. S3) (change in the NME_T of 1.5%) and the uncertainty of the

519   estimates (change in the $ARSD$ of 2.5%). The error in the estimated areogram was also

520   small but in this case the error increased by 5%. The additional data point helped

521   decrease the errors for the estimated mass of the more volatile SOA products (Fig. 9)

522   and especially for the 10^2 μg m^{-3} bin. The ΔH_{vap} and α_m estimated values were only

523   slightly affected by the additional measurement.

524   These results suggest that an additional yield measurement at high SOA can

525   lead to a substantial reduction of the error for the estimated yields at low temperatures

526   (Fig. 10) and also a better estimation of the SOA products with higher volatility (10^2

527   and 10^3 μg m^{-3}). These products may contribute little to the SOA concentration at 25

528   °C, but their reactions (aging) could lead to significant additional SOA in later stages.

529

5. Conclusions

531   An algorithm was developed to estimate VBS parameters for SOA formation

532   combining yield measurements from atmospheric simulation chambers with

533   thermodenuder and isothermal dilution measurements chambers. An additional feature

534   of this approach is that the algorithm estimates the uncertainty of the predicted SOA

535   yields for different SOA concentrations and temperatures, assisting in this way in the

536   design of future experiments.

537   The algorithm was evaluated against pseudo-experimental data for SOA

538   systems with known properties. The algorithm performed quite well at reproducing the

539   SOA yields at atmospherically relevant concentrations and temperatures with errors

540   less than 20% for practically all cases. This was the case even at temperatures as low

541   as 5 °C and also when the volatility range used for the parameter estimation was

542   narrower than that of the simulated SOA system. One should note that this error was

543   quite similar in most cases to the experimental error assumed in the construction of the

544   "measurement" datasets.

545   The errors in the retrieved SOA volatility distributions were in general higher

546   than those of the SOA yields. This is due to a large extent to the existence of multiple

547   solutions that can result in similar yields. The accuracy of the estimated mass fractions

548   of the more volatile SOA components improved when an additional yield measurement

549   at high SOA (e.g., at 200 μg m^{-3}). The addition of this measurement also improved the

550   estimated yields at low temperatures. This therefore suggests that data points at high

551   SOA concentrations should also be obtained experimentally, together with the data

552   points at atmospherically relevant atmospheric SOA levels.

553   In all cases the algorithm results in good estimates of the effective evaporation

554   enthalpy. On the other hand, the estimates of the effective accommodation coefficient

555   are usually quite uncertain.

556   The approach combining yield, TD (thermograms), and isothermal dilution

557   (areograms) measurements is recommended for future parametrizations of SOA

558   formation.

559

560   **6. Code and data availability**

561   The   code   and   simulation   results   are   available   upon   request

562   (spyros@chemeng.upatras.gr).

563

564   **7. Supplementary information**

565

566   **8. Author contribution**

567   PU, and SNP designed the research. PU developed the final model code. AD developed

568   a first version of the code and performed preliminary feasibility tests. DS and SNP

569   designed the experiments for the α-humulene ozonolysis and DS carried them out. PU

570   performed the simulations, the formal analysis, and wrote the original draft. Paper

571   review and editing was performed by SNP.

572

573   **9. Competing interests**

574   The authors declare that they have no conflict of interest.

575

576   **10. Financial support**

577   This work has been supported by the Chemical evolution of gas and particulate-phase

578   organic pollutants in the atmosphere (CHEVOPIN) Project of the Hellenic Foundation

579   for Research and Innovation (HFRI) under grant agreement no. 1819 and the European

580 Union's Horizon 2020 research and innovation program through the EUROCHAMP-
581 2020 Infrastructure Activity under grant agreement no. 730997.

582

11. References

583 **11. References**

584 An, W. J., Pathak, R. K., Lee, B. H. and Pandis, S. N.: Aerosol volatility measurement
585   using an improved thermodenuder: Application to secondary organic aerosol, J.
586   Aerosol Sci., 38, 305–314, doi:10.1016/j.jaerosci.2006.12.002, 2007.

587 Baltensperger, U., Kalberer, M., Dommen, J., Paulsen, D., Alfarra, M. R., Coe, H.,
588   Fisseha, R., Gascho, A., Gysel, M., Nyeki, S., Sax, M., Steinbacher, M., Prevot, A.
589   S. H., Sjögren, S., Weingartner, E. and Zenobi, R.: Secondary organic aerosols from
590   anthropogenic and biogenic precursors, Faraday Discuss., 130, 265–278,
591   doi:10.1039/b417367h, 2005.

592 Burtscher, H., Baltensperger, U., Bukowiecki, N., Cohn, P., Hüglin, C., Mohr, M.,
593   Matter, U., Nyeki, S., Schmatloch, V., Streit, N. and Weingartner, E.: Separation of
594   volatile and non-volatile aerosol fractions by thermodesorption: Instrumental
595   development and applications, J. Aerosol Sci., 32, 427–442, doi:10.1016/S0021-
596   8502(00)00089-6, 2001.

597 Cain, K. P., Karnezi, E. and Pandis, S. N.: Challenges in determining atmospheric
598   organic aerosol volatility distributions using thermal evaporation techniques,
599   Aerosol Sci. Technol., 54, 941–957, doi:10.1080/02786826.2020.1748172, 2020.

600 Cappa, C. D.: A model of aerosol evaporation kinetics in a thermodenuder, Atmos.
601   Meas. Tech., 3, 579–592, doi:10.5194/amt-3-579-2010, 2010.

602 Cappa, C. D. and Jimenez, J. L.: Quantitative estimates of the volatility of ambient
603   organic aerosol, Atmos. Chem. Phys., 10, 5409–5424, doi:10.5194/acp-10-5409-
604   2010, 2010.

605 Donahue, N. M., Robinson, A. L., Stanier, C. O. and Pandis, S. N.: Coupled
606   partitioning, dilution, and chemical aging of semivolatile organics, Environ. Sci.
607   Technol., 40, 2635–2643, doi:10.1021/es052297c, 2006.

608 Emery, C., Liu, Z., Russell, A. G., Odman, M. T., Yarwood, G., and Kumar, N.:
609   Recommendations on statistics and benchmarks to assess photochemical model
610   performance, J. Air Waste Manag. Assoc., 67, 582–598,
611   https://doi.org/10.1080/10962247.2016.1265027, 2017.

612 Fuchs, N. A. and Sutugin, A. G.: Highly Dispersed Aerosols, Ann Arbor Science
613   Publishers, Ann Arbor, London., 1970.

614   Fuentes, E. and McFiggans, G.: A modeling approach to evaluate the uncertainty in
615   estimating the evaporation behaviour and volatility of organic aerosols, Atmos.
616   Meas. Tech., 5, 735–757, doi:10.5194/amt-5-735-2012, 2012.

617   Grieshop, A. P., Miracolo, M. A., Donahue, N. M. and Robinson, A. L.: Constraining
618   the volatility distribution and gas-particle partitioning of combustion aerosols using
619   isothermal dilution and thermodenuder measurements, Environ. Sci. Technol., 43,
620   4750–4756, doi:10.1021/es8032378, 2009.

621   Huffman, J. A., Docherty, K. S., Mohr, C., Cubison, M. J., Ulbrich, I. M., Ziemann, P.
622   J., Onasch, T. B. and Jimenez, J. L.: Chemically-resolved volatility measurements
623   of organic aerosol from different sources, Environ. Sci. Technol., 43, 5351–5357,
624   doi:10.1021/es803539d, 2009.

625   IPCC: Climate Change 2013: The Physical Science Basis. Contribution of Working
626   Group I to the Fifth Assessment Report of the Intergovernmental Panel on Climate
627   Change, Cambridge., 2013.

628   Kalberer, M., Paulsen, D., Sax, M., Steinbacher, M., Dommen, J., Prevot, A. S. H.,
629   Fisseha, R., Weingartner, E., Frankevich, V., Zenobi, R. and Baltensperger, U.:
630   Identification of polymers as major components of atmospheric organic aerosols,
631   Science, 303, 1659–1662, doi:10.1126/science.1092185, 2004.

632   Kanakidou, M., Seinfeld, J. H., Pandis, S. N., Barnes, I., Dentener, F. J., Facchini, M.
633   C., Van Dingenen, R., Ervens, B., Nenes, A., Nielsen, C. J., Swietlicki, E., Putaud,
634   J. P., Balkanski, Y., Fuzzi, S., Horth, J., Moortgat, G. K., Winterhalter, R., Myhre,
635   C. E. L., Tsigaridis, K., Vignati, E., Stephanou, E. G. and Wilson, J.: Organic
636   aerosol and global climate modelling: A review, Atmos. Chem. Phys., 5, 1053–
637   1123, doi:10.5194/acp-5-1053-2005, 2005.

638   Karnezi, E., Riipinen, I. and Pandis, S. N.: Measuring the atmospheric organic aerosol
639   volatility distribution: A theoretical analysis, Atmos. Meas. Tech., 7, 2953–2965,
640   doi:10.5194/amt-7-2953-2014, 2014.

641   Lane, T. E., Donahue, N. M. and Pandis, S. N.: Effect of NO_x on secondary organic
642   aerosol   concentrations,   Environ.   Sci.   Technol.,   42,   6022–6027,
643   doi:10.1021/es703225a, 2008.

644   Lee, B. H., Kostenidou, E., Hildebrandt, L., Riipinen, I., Engelhart, G. J., Mohr, C.,
645   Decarlo, P. F., Mihalopoulos, N., Prevot, A. S. H., Baltensperger, U. and Pandis, S.
646   N.: Measurement of the ambient organic aerosol volatility distribution: Application

647   during the Finokalia Aerosol Measurement Experiment (FAME-2008), Atmos.
648   Chem. Phys., 10, 12149–12160, doi:10.5194/acp-10-12149-2010, 2010.
649 Lee, B. H., Pierce, J. R., Engelhart, G. J. and Pandis, S. N.: Volatility of secondary
650   organic aerosol from the ozonolysis of monoterpenes, Atmos. Environ., 45, 2443–
651   2452, doi:10.1016/j.atmosenv.2011.02.004, 2011.
652 Lim, S. S., Vos, T., Flaxman, A. D., Danaei, G., Shibuya, K., Adair-Rohani, H., Amann,
653   M., Anderson, H. R., Andrews, K. G., Aryee, M., Atkinson, C., Bacchus, L. J.,
654   Bahalim, A. N., Balakrishnan, K., Balmes, J., Barker-Collo, S., Baxter, A., Bell, M.
655   L., Blore, J. D., Blyth, F., Bonner, C., Borges, G., Bourne, R., Boussinesq, M.,
656   Brauer, M., Brooks, P., Bruce, N. G., Brunekreef, B., Bryan-Hancock, C., Bucello,
657   C., Buchbinder, R., Bull, F., Burnett, R. T., Byers, T. E., Calabria, B., Carapetis, J.,
658   Carnahan, E., Chafe, Z., Charlson, F., Chen, H., Chen, J. S., Cheng, A. T. A., Child,
659   J. C., Cohen, A., Colson, K. E., Cowie, B. C., Darby, S., Darling, S., Davis, A.,
660   Degenhardt, L., Dentener, F., Des Jarlais, D. C., Devries, K., Dherani, M., Ding, E.
661   L., Dorsey, E. R., Driscoll, T., Edmond, K., Ali, S. E., Engell, R. E., Erwin, P. J.,
662   Fahimi, S., Falder, G., Farzadfar, F., Ferrari, A., Finucane, M. M., Flaxman, S.,
663   Fowkes, F. G. R., Freedman, G., Freeman, M. K., Gakidou, E., Ghosh, S.,
664   Giovannucci, E., Gmel, G., Graham, K., Grainger, R., Grant, B., Gunnell, D.,
665   Gutierrez, H. R., Hall, W., Hoek, H. W., Hogan, A., Hosgood, H. D., Hoy, D., Hu,
666   H., Hubbell, B. J., Hutchings, S. J., Ibeanusi, S. E., Jacklyn, G. L., Jasrasaria, R.,
667   Jonas, J. B., Kan, H., Kanis, J. A., Kassebaum, N., Kawakami, N., Khang, Y. H.,
668   Khatibzadeh, S., Khoo, J. P., Kok, C., et al.: A comparative risk assessment of
669   burden of disease and injury attributable to 67 risk factors and risk factor clusters
670   in 21 regions, 1990-2010: A systematic analysis for the Global Burden of Disease
671   Study 2010, Lancet, 380, 2224–2260, doi:10.1016/S0140-6736(12)61766-8, 2012.
672 Louvaris, E. E., Florou, K., Karnezi, E., Papanastasiou, D. K., Gkatzelis, G. I. and
673   Pandis, S. N.: Volatility of source apportioned wintertime organic aerosol in the
674   city of Athens, Atmos. Environ., 158, 138–147, doi:10.1016/j.atmosenv.2017.
675   03.042, 2017a.
676 Louvaris, E. E., Karnezi, E., Kostenidou, E., Kaltsonoudis, C. and Pandis, S. N.:
677   Estimation of the volatility distribution of organic aerosol combining
678   thermodenuder and isothermal dilution measurements, Atmos. Meas. Tech., 10,
679   3909–3918, doi:10.5194/amt-10-3909-2017, 2017b.

680 Odum, J. R., Hoffmann, T., Bowman, F., Collins, D., Flagan, R. C. and Seinfeld, J. H.:
681   Gas/particle partitioning and secondary organic aerosol yields, Environ. Sci.
682   Technol., 30, 2580–2585, doi:10.1021/es950943+, 1996.

683 Pankow, J. F.: An absorption model of gas/particle partitioning of organic compounds
684   in the atmosphere, Atmos. Environ., 28, 185–188, doi:10.1016/1352-
685   2310(94)90093-0, 1994a.

686 Pankow, J. F.: An absorption model of the gas/aerosol partitioning involved in the
687   formation of secondary organic aerosol, Atmos. Environ., 28, 189–193,
688   doi:10.1016/1352-2310(94)90094-9, 1994b.

689 Pathak, R. K., Stanier, C. O., Donahue, N. M. and Pandis, S. N.: Ozonolysis of α-pinene
690   at atmospherically relevant concentrations: Temperature dependence of aerosol
691   mass fractions (yields), J. Geophys. Res., 112, 1–8, doi:10.1029/2006JD007436,
692   2007a.

693 Pathak, R. K., Presto, A. A., Lane, T. E., Stanier, C. O., Donahue, N. M. and Pandis, S.
694   N.: Ozonolysis of α-pinene: Parameterization of secondary organic aerosol mass
695   fraction, Atmos. Chem. Phys., 7, 3811–3821, doi:10.5194/acp-7-3811-2007,
696   2007b.

697 Pope, C. A. and Dockery, D. W.: Health effects of fine particulate air pollution: Lines
698   that connect, J. Air Waste Manag. Assoc., 56, 709–742,
699   doi:10.1080/10473289.2006.10464485, 2006.

700 Riipinen, I., Pierce, J. R., Donahue, N. M. and Pandis, S. N.: Equilibration time scales
701   of organic aerosol inside thermodenuders: Evaporation kinetics versus
702   thermodynamics, Atmos. Environ., 44, 597–607, doi:10.1016/j.atmosenv.
703   2009.11.022, 2010.

704 Seinfeld, J. H. and Pandis, S. N.: Atmospheric Chemistry and Physics: From Air
705   Pollution to Climate Change, Third., John Wiley & Sons, Hoboken, New Jersey.,
706   2016.

707 Sippial, D., Uruci, P., Kostenidou, E. and Pandis, S. N.: Formation of secondary organic
708   aerosol during the dark-ozonolysis of α-humulene, submitted for publication, 2023.

709 Stanier, C. O., Pathak, R. K. and Pandis, S. N.: Measurements of the volatility of
710   aerosols from α-pinene ozonolysis, Environ. Sci. Technol., 41, 2756–2763,
711   doi:10.1021/es0519280, 2007.

712 Stanier, C. O., Donahue, N. and Pandis, S. N.: Parameterization of secondary organic

713   aerosol mass fractions from smog chamber data, Atmos. Environ., 42, 2276–2299,

714   doi:10.1016/j.atmosenv.2007.12.042, 2008.

715 Strader, R., Lurmann, F. and Pandis, S. N.: Evaluation of secondary organic aerosol

716   formation in winter, Atmos. Environ., 33, 4849–4863, doi:10.1016/S1352-

717   2310(99)00310-6, 1999.

718 Wehner, B., Philippin, S. and Wiedensohler, A.: Design and calibration of a

719   thermodenuder with an improved heating unit to measure the size-dependent

720   volatile fraction of aerosol particles, J. Aerosol Sci., 33, 1087–1093,

721   doi:10.1016/S0021-8502(02)00056-3, 2002.

722 Zhang, Q., Jimenez, J. L., Canagaratna, M. R., Allan, J. D., Coe, H., Ulbrich, I., Alfarra,

723   M. R., Takami, A., Middlebrook, A. M., Sun, Y. L., Dzepina, K., Dunlea, E.,

724   Docherty, K., DeCarlo, P. F., Salcedo, D., Onasch, T., Jayne, J. T., Miyoshi, T.,

725   Shimono, A., Hatakeyama, S., Takegawa, N., Kondo, Y., Schneider, J., Drewnick,

726   F., Borrmann, S., Weimer, S., Demerjian, K., Williams, P., Bower, K., Bahreini, R.,

727   Cottrell, L., Griffin, R. J., Rautiainen, J., Sun, J. Y., Zhang, Y. M. and Worsnop, D.

728   R.: Ubiquity and dominance of oxygenated species in organic aerosols in

729   anthropogenically-influenced Northern Hemisphere midlatitudes, Geophys. Res.

730   Lett., 34, 1–6, doi:10.1029/2007GL029979, 2007.

731

732

733

Table 1: True and estimated volatility distribution of the products for 8 different tests. The uncertainty of the estimates ($\pm\sigma$) is also included.

TEST	ΔH_{vap} (kJ mol^{-1})	$log(\alpha_m)$	Stoichiometric Coefficients (α_i) at C_i^* (µg m^{-3})						
			10^{-2}	10^{-1}	10^0	10^1	10^2	10^3	10^4
True A	30	-0.30	-	-	0.070	0.038	0.179	0.300	-
A1	32.9±9.6	-0.77±0.47	-	-	0.059 ±0.022	0.071 ±0.052	0.252 ±0.130	0.255 ±0.191	-
A2	32.0±9.8	-0.72±0.45	-	-	0.062 ±0.021	0.067 ±0.053	0.286 ±0.132	-	-
A3	32.0±9.8	-0.72±0.45	-	0.000 ±0.000	0.062 ±0.021	0.067 ±0.053	0.286 ±0.132	-	-
A4	34.0±9.2	-0.70±0.46	-	-	0.062 ±0.021	0.082 ±0.050	0.191 ±0.084	0.259 ±0.198	-
True B	30	-0.30	0.001	0.012	0.037	0.088	0.099	0.250	0.800
B1	33.8±9.2	-0.95±0.21	-	-	0.052 ±0.011	0.037 ±0.039	0.374 ±0.122	0.226 ±0.176	-
B2	36.5±7.6	-0.93±0.26	-	-	0.050 ±0.000	0.051 ±0.039	0.292 ±0.103	0.234 ±0.196	-
True C	115	-2.02	0.118	0.094	0.116	0.247	-	-	-
C1	104.6±24.0	-1.74±0.97	0.126 ±0.086	0.116 ±0.090	0.154 ±0.116	0.216 ±0.126	-	-	-
C2	91.2±19.2	-2.36±0.83	-	-	0.415 ±0.099	0.143 ±0.117	0.137 ±0.113	0.115 ±0.095	-

Table 2: The *mean normilized error* (MNE) between the "measurements" and "true" values, and between the "measurements" and the model estimated values for the different tests.

Test	"Measurements" vs "True" [a]			"Measurements" vs Estimated MNE_M [b]		
	Yield	**TD**	**Dilution**	**Yield**	**TD**	**Dilution**
A1	21.2	7.6	9.4	25.0	7.0	16.69
A2	21.2	7.6	9.4	25.1	7.1	16.71
A3	21.2	7.6	9.4	25.1	7.1	16.71
A4	17.8	7.6	9.4	22.4	7.1	19.7
B1	20.5	6.9	5.6	20.6	6.0	14.7
B2	18.1	6.9	5.6	19.1	7.8	18.1
C1	8.4	11.6	1.8	6.3	12.9	3.5
C2	8.4	11.6	1.8	8.6	32.4	2.3

[a] Calculated by $\dfrac{100}{N_O} \sum\limits_{i=1}^{N_O} \dfrac{|O_i - TR_i|}{O_i}$.

[b] Calculated by Eq. (16).

Table 3: The *mean normilized error* between the "true" and estimated values (MNE_T) for the different tests.

Test	Yield				TD	Dilution
	5 ºC	15 ºC	25 ºC	35 ºC		
A1	24.4	21.0	17.3	13.8	5.5	19.0
A2	21.4	19.5	16.9	14.1	4.7	18.5
A3	21.4	19.5	16.9	14.1	4.7	18.5
A4	20.4	18.3	15.7	12.9	6.0	22.5
B1	31.3	21.7	13.9	8.7	4.0	13.3
B2	24.4	15.6	9.0	6.4	2.5	18.4
C1	6.2	6.8	9.6	15.5	4.4 (110 ºC)[*] 10.6 (140 ºC)[*]	2.7
C2	18.1	9.6	7.2	11.5	9.0 (110 ºC)[*] 27.8 (140 ºC)[*]	3.4

[*] The errors for TD were calculated up to the denoted temperature in the parenthesis.

Table 4: The average relative standard deviation (*ARSD*) for the different tests.

Test	Yield				TD	Dilution
	5 ºC	15 ºC	25 ºC	35 ºC		
A1	34.6	29.7	26.0	24.2	21.0	23.6
A2	32.1	28.5	25.2	23.3	21.1	23.2
A3	32.1	28.5	25.2	23.3	21.1	23.2
A4	30.8	27.2	24.5	23.3	21.0	22.1
B1	37.1	27.2	20.0	16.9	20.5	18.0
B2	33.8	25.0	18.5	15.7	18.0	15.9
C1	15.0	14.9	16.2	22.9	20.7[*]	16.5
C2	20.1	15.6	14.1	21.3	20.6[*]	9.8

[*] The *ARSD* for the TD MFR values were calculated in the 20–120 ºC temperature range.
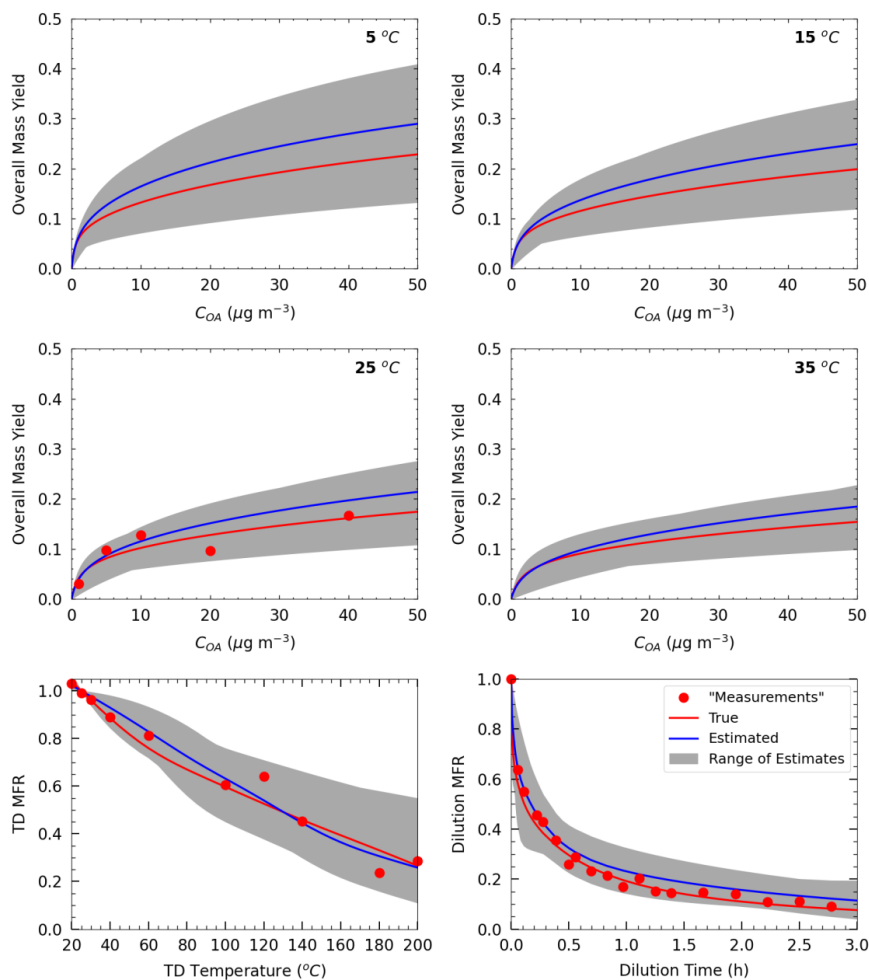
Figure 1: "Measurements" of Test A1 in Experiment A (red dots), true (red line) and estimated (blue line) yields at four temperatures (at 5 °C, 15 °C, 25 °C, and 35 °C), TD (thermogram), and dilution (areogram) values. The grey area shows the range of good solutions obtained by our algorithm.
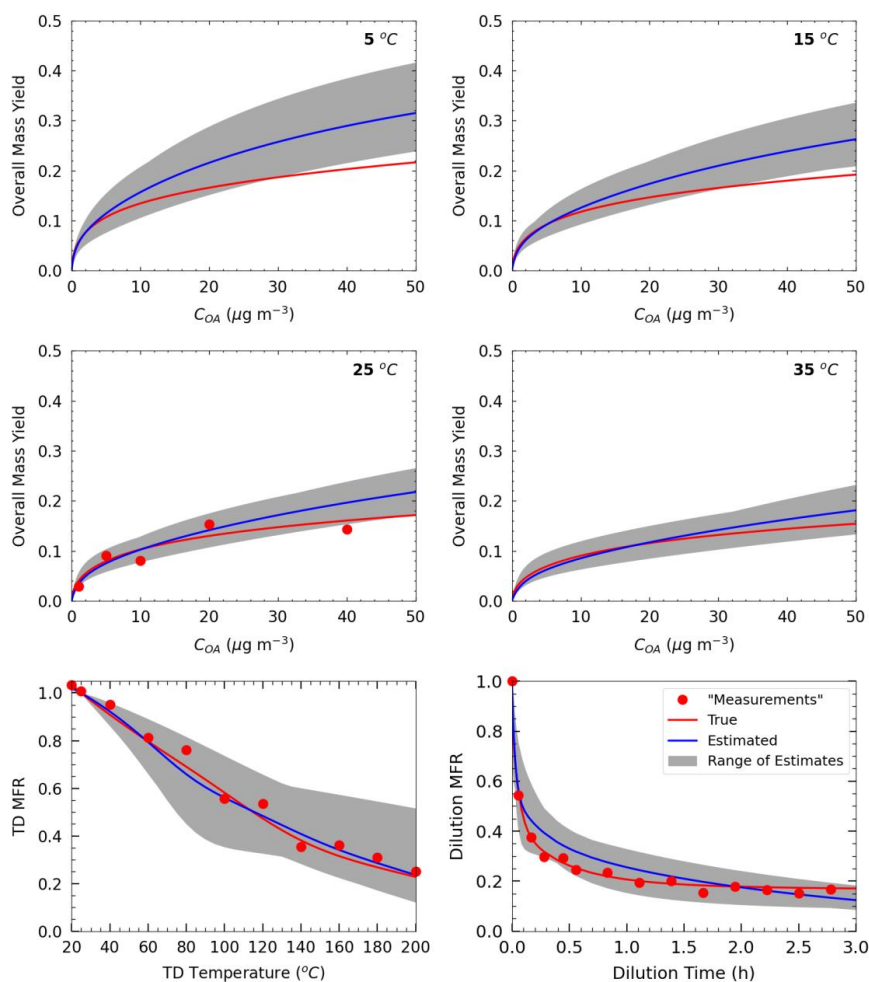
Figure 2: "Measurements" of Test B1 in Experiment B (red dots), true (red line) and estimated (blue line) yields at four temperatures (at 5 ºC, 15 ºC, 25 ºC, and 35 ºC), TD (thermogram), and dilution (areogram) values. The grey area shows the range of good solutions.
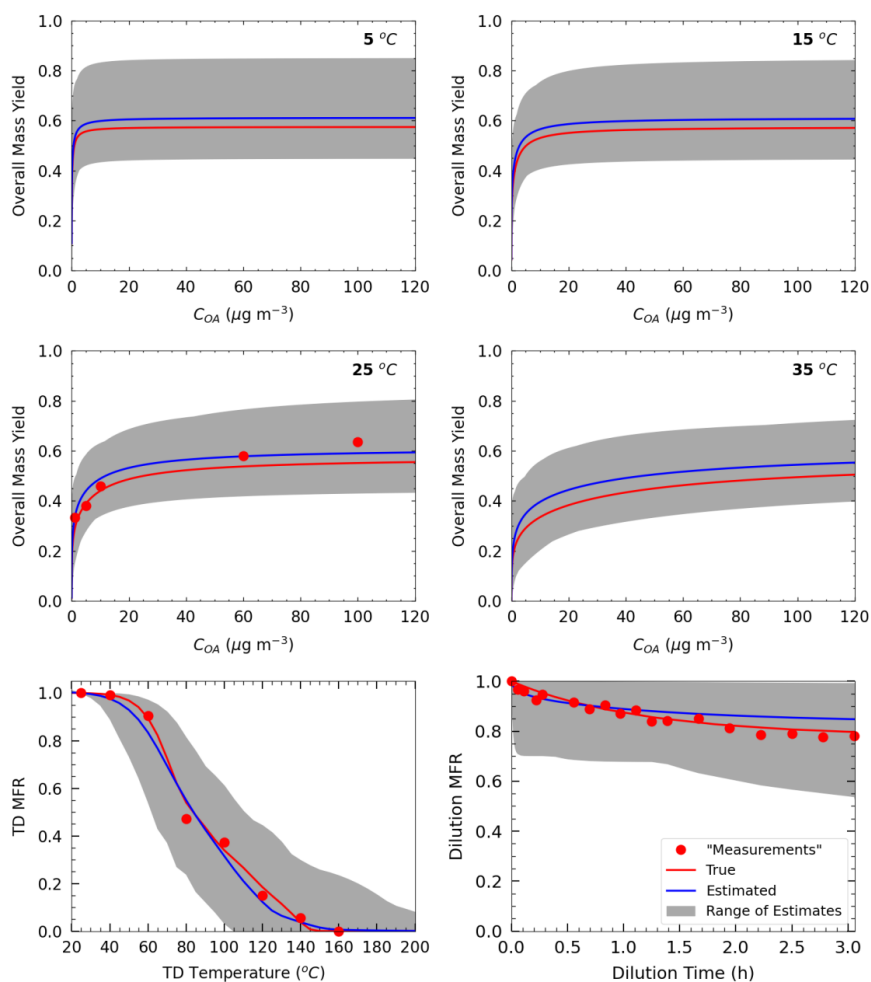
Figure 3: "Measurements" of Test C1 in Experiment C (red dots), true (red line) and estimated (blue line) yields at four temperatures (at 5 °C, 15 °C, 25 °C, and 35 °C), TD (thermogram), and dilution (areogram) values. The grey area shows the range of good solutions.
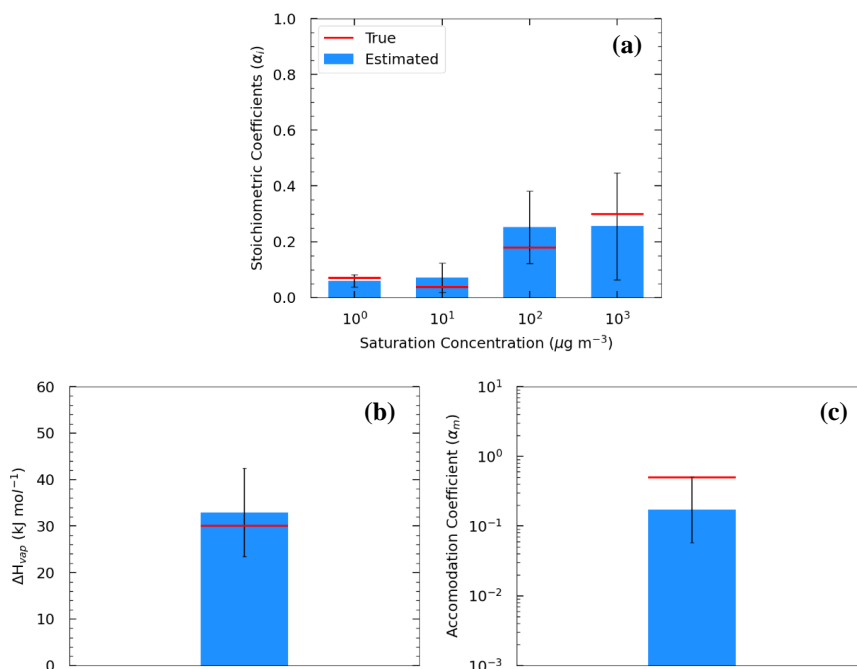
Figure 4. Estimated (bars) and true (red lines) parameter values of Experiment A in Test A1 combining yield, TD, and isothermal dilution measurements for: **(a)** the volatility distribution of the products, **(b)** ΔH_{vap}, and **(c)** α_{m}. The error bars represent the uncertainty of the estimated values.
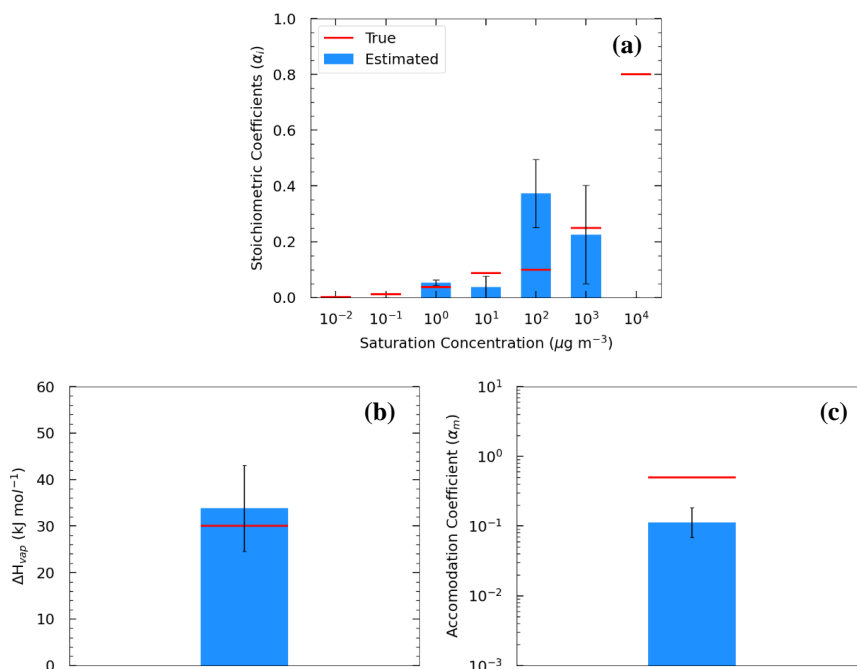
Figure 5: Estimated (bars) and true (red lines) parameter values of Experiment B in Test B1 combining yield, TD, and isothermal dilution measurements for: **(a)** the volatility distribution of the products, **(b)** ΔH_{vap}, and **(c)** α_m. The error bars represent the uncertainty of the estimated values.
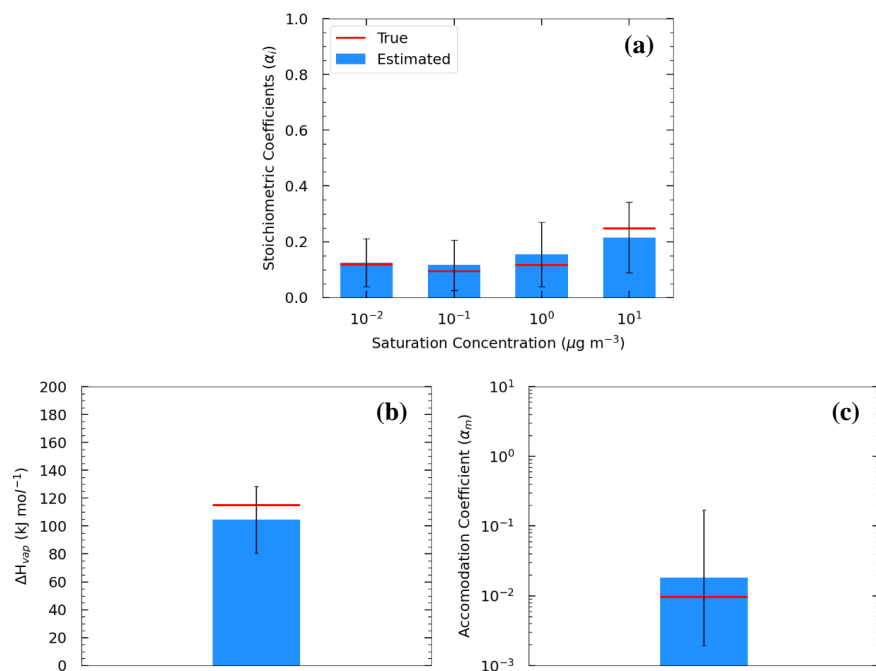
Figure 6: Estimated (bars) and true (red lines) parameter values of Experiment C in Test C1 combining yield, TD, and isothermal dilution measurements for: **(a)** the volatility distribution of the products, **(b)** ΔH_{vap}, and **(c)** α_m. The error bars represent the uncertainty of the estimated values.
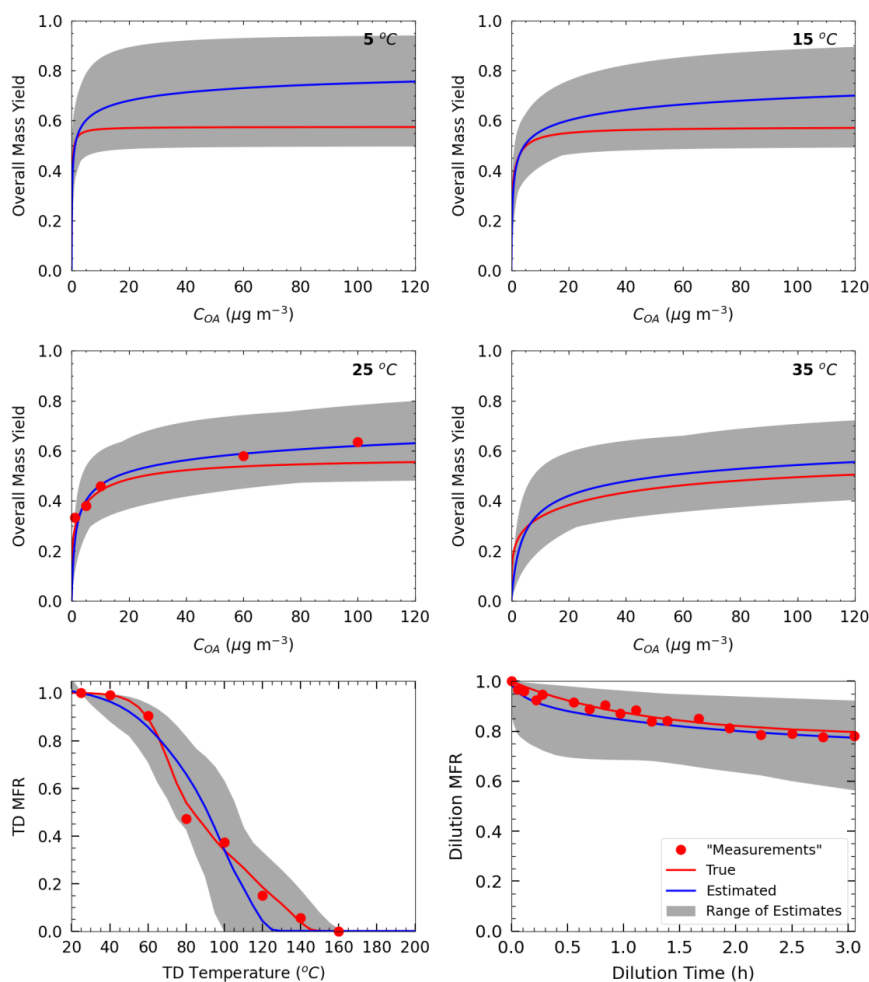
Figure 7: Yields calculated using the "true" parameters of Experiment C (red line) and the estimated (blue line) using the parameters of Test C2 for the following temperatures: 5 °C, 15 °C, 25 °C, and 35 °C. Also shown the thermogram and aerogram. The grey area shows the range of good solutions obtained by our algorithm.
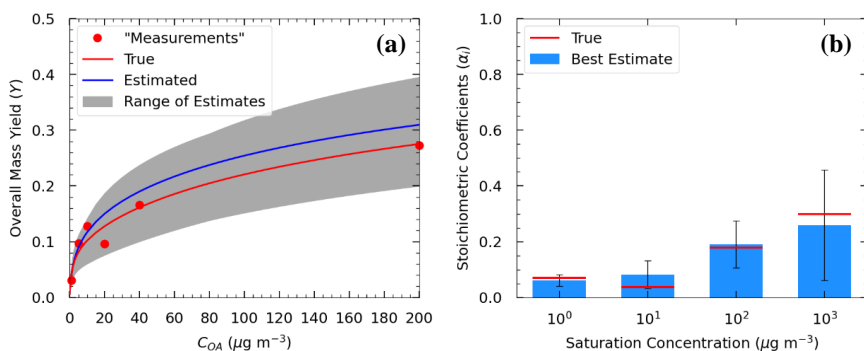
Figure 8: (a) True (red line) and estimated (blue line) yields in Test A4, and the "measurements" of Experiment A (red dots) including an additional yield "measurement" at 200 µg m⁻³. **(b)** Estimated volatility distribution of the products (bars) of Test A4 and the true (red lines) parameter values.
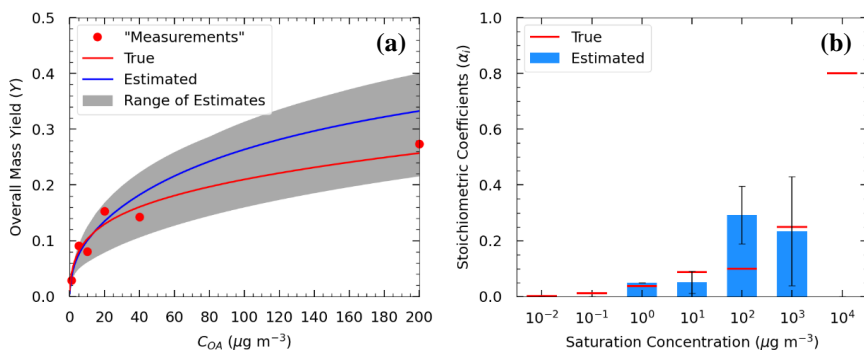
Figure 9: (a) Estimated yields (blue line) in Test B2 and "measurements" of Experiment B (red dots) including an additional yield "measurement" at 200 µg m⁻³. **(b)** Estimated volatility distribution of the products (bars) of Test B2 and the true (red lines) parameter values.
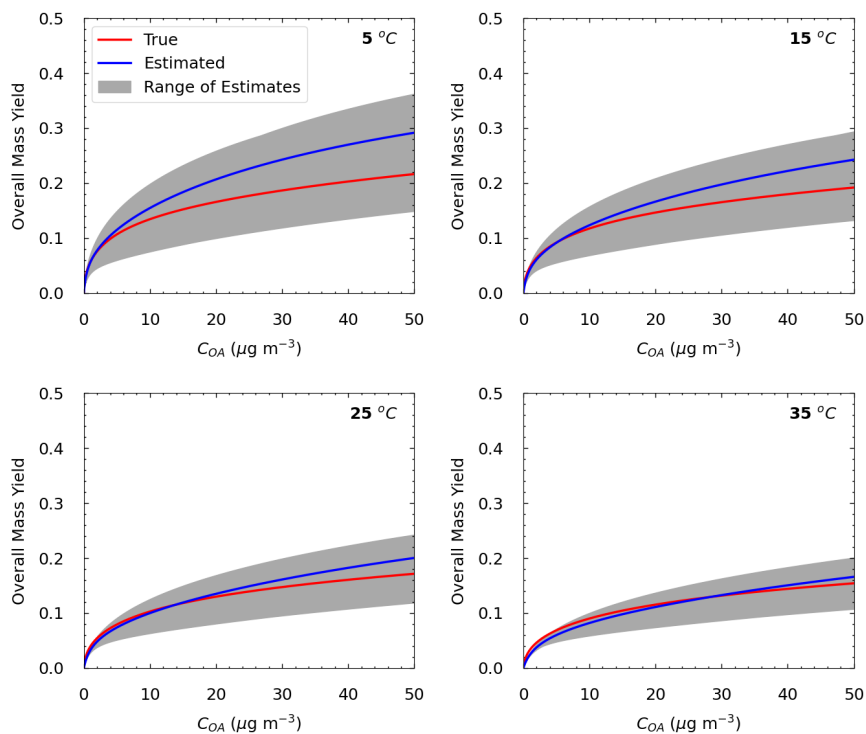
Figure 10: Yields calculated using the "true" parameters of Experiment B (red line) and the estimated (blue line) using the parameters of Test B2 for the following temperatures: 5 ℃, 15 ℃, 25 ℃, and 35 ℃. The grey area shows the range of good solutions obtained by our algorithm.